A&A 509, A56 (2010)
DOI: 10.1051/0004-6361/200912952

Astronomy & Astrophysics

H Lyman α line in Jovian aurorae: electron transport and radiative transfer coupled modelling

H. Menager, M. Barthélemy, and J. Lilensten

Laboratoire de Planétologie de Grenoble, BP 53, 38041 Grenoble Cedex 1, France
e-mail: helene.menager@obs.ujf-grenoble.fr

Received 27 July 2009 / Accepted 10 November 2009

ABSTRACT

Aims. The aim of this work is to characterize the impact of the solar UV flux and of the electron precipitation on Jupiter's atmosphere and to study the H Lyman α intensity and spectral profile in Jupiter's aurorae. In particular we characterize the sensitivity of the line to the relevant input parameters.
Methods. We use a multi-stream electron transport code solving the 1D Boltzmann equation and a Feautrier technique radiative transfer code.
Results. We calculate ionization rate profiles of the main species of Jupiter's ionosphere and the heating rate due to electron precipitation, as a function of the energy of the precipitation. We also calculate the emission rate of Lyman α photons under auroral electron precipitation and the ensuing line profile. The profile exhibits a centre reversal which could be used as a diagnostic of Jupiter's auroral low-energy electron precipitation.

Key words. planets and satellites: individual: Jupiter – plasmas – radiation transfer – line: profiles – ultraviolet: planetary systems – radiation mechanisms: non thermal

1. Introduction

The permanent aurorae on Jupiter are due to the precipitation of plasma along magnetic field lines, from the magnetosphere into the upper atmosphere. The charged particles excite and ionize the neutral atmospheric species through collisions. The ensuing radiative de-excitation of the atmospheric species produces aurorae. In spite of the presence of precipitated ions, energetic electrons play the leading role in Jupiter's auroral processes (Trafton et al. 1998; Rego et al. 2001). These particles carry a considerable power, estimated to 10^{13}–10^{14} W (Rego et al. 1994). The solar UV flux also excites and ionizes the atmosphere but it carries 100 times less power than the precipitating electrons.

Several observable quantities are helpful to study the aurorae. In the infrared, H_3^+ emissions are very bright and provide information on the thermal stucture and dynamics (Miller et al. 2000). The visible spectrum has interesting features due to H_2 and the Balmer series of H (Vasavada et al. 1999). The brightest auroral emissions are in the UV range: the H Lyman α line at 121.567 nm and the H_2 Lyman and Werner bands between 90 and 170 nm. They have been observed with the Goddard High Resolution Spectrograph and the Space Telescope Imaging Spectrograph on HST (Rego et al. 2001; Ben Jaffel et al. 2007). They are used to investigate the nature of the precipitating particles and the thermal structure of the atmosphere. In this work we focus on the Lyman α radiation and investigate which quantities can be constrained by its study.

Several authors studied the auroral ionosphere and calculated ion production profiles and UV emission rates of H and H_2. Some used the rough continuous slowing down approximation and modelled the impact of precipitating electrons and protons (Rego et al. 1994; Prangé et al. 1995). Others solved more accurate kinetic transport equations to study the impact of the precipitating electrons. Perry et al. (1999) used a multi-stream code to investigate the impact of the solar UV radiation and electron precipitation on a model atmosphere. Their atmosphere model was built on data from Galileo and Voyager, which is not well suited to describe the auroral atmosphere. Grodent & Gérard (2001) solved transport and diffusion equations with a 2-stream code, calculating self-consistently an atmosphere model adapted to auroral regions. Prangé et al. (1995) showed that a color ratio in H_2 spectrum, which is linked with the absorption by hydrocarbons, strongly depends on the angular distribution of electrons, demonstrating the limits of 2-stream calculations.

In this work we study the effect of the solar EUV flux and of the electrons precipitating in the auroral atmosphere by using a multi-stream kinetic transport code and an adequate auroral atmosphere model associated with updated cross sections. We thus calculate the ionization and excitation rates and the Lyman α photons production rate. A radiative transfer code is then developed to model the emergent Lyman α line profile in an optically thick atmosphere. Rego et al. (1999) used a radiative transfer code based on the "doubling and adding" method (Ben Jaffel et al. 2007). The frequency shift that can occur during a diffusion was described with the use of frequency redistribution functions. They tested the angle-averaged partial redistribution function, which is suitable in a low collisional atmosphere, and the complete frequency redistribution function, which is adequate for a dense atmosphere. In our work we use a radiative transfer code based on the Feautrier method to compute the emergent Lyman α line shape and intensity. We use the frequency redistribution functions cited above.

2. Modelling electron transport

2.1. Kinetic transport code

We have adapted the TRANS* kinetic transport code to model the jovian auroral ionosphere. This code is described in Lilensten & Blelly (2002). It computes the impact of the solar EUV flux

and of auroral electrons on the ionosphere. It calculates the suprathermal electron flux by solving the 1D Boltzmann stationary equation. This flux is due to the photoproduction of primary electrons and to the collisions between the atmospheric gas with primary photoelectrons or precipitated electrons which produce "secondary electrons". The code provides ion production rates, excitation rates of the atmospheric neutral species and heating rates. TRANS* has proven its robustness in modelling the ionospheres of the Earth, Mars, Venus and Titan (Lilensten & Blelly 2002; Lilensten et al. 2005; Gronoff et al. 2008).

2.1.1. Modelling with TRANS*

Once the source term of the Boltzmann equation is evaluated, this equation is similar to a radiative transfer equation. The code solves it with the discrete ordinates method. It relies on several assumptions. We suppose that the precipitation and the atmosphere are in a stationary state. This is justified by the fact that the incident auroral energy is absorbed in a time too short for the precipitation to vary. We make a pseudo-1D modelling. This prevents us from studying the horizontal transport of particles but is adequate to describe the precipitation of particles along the magnetic field lines. We neglect the electric and gravity forces. Actually the electric field could accelerate the electrons and deviate them from their motion around the magnetic field lines, which would modify the altitude at which they are absorbed but this field is still unknown. Moreover we describe the dissipative effects in the suprathermal electron flux with a continuous loss function (Stamnes & Rees 1983). Eventually, we need to improve the classical TRANS* code to include relativistic effects. We must keep this in mind when we study the precipitation of high-energy electrons. Electrons of 3 keV have a speed of $0.1c$; our classical treatment reaches its limits there.

2.1.2. Angle, altitude and energy discretization

The atmosphere is described with a non-uniform spatial grid. Since the atmosphere is not isothermal, the scale height H varies with altitude, from $H = 25$ km at $z = 110$ km (above the 1 bar level) to $H = 230$ km on top of the atmosphere. To take this variation into account, the spatial grid step varies exponentially with altitude, going from 1 km at $z = 110$ km to 50 km on top of the atmosphere. The atmosphere is described with a series of 160 isothermal and homogenous layers. We also use a numerical grid to describe the angular distribution of electrons: TRANS* is a "multi-stream" model. 8 streams are enough to make an accurate description. One Gaussian weight is attributed to each angle. Finally, we use a power law grid for the energy discretization. We use up to 900 energy bins in which we distribute the electrons.

2.1.3. Atmosphere model

The first input of the code is an atmosphere model: we need a temperature profile and density profiles of the main neutral species. No temperature profile has been measured in auroral regions. The only in situ temperature measurement was done by the Galileo probe at a latitude of 6° (Seiff et al. 1998). In auroral regions, only spectroscopic observations of hydrocarbons, H_2 and H_3^+ bands constrain the temperature profile (Trafton et al. 1994; Stallard et al. 2002). The density profiles of the atmospheric species in polar regions are not very well known either. Our model includes the four most abundant species in Jupiter's upper atmosphere: H, H_2, He and CH_4. At low latitude, Voyager made some occultation measurements of H and H_2 concentrations and Galileo measured mixing ratios of the most abundant species in the atmosphere (Young 2003). Several authors built auroral atmospheric models based on these data. Trafton et al. (1994) elaborated a model which allows to build synthetic spectra reproducing the Lyman and Werner bands of H_2. In this model, the exospheric temperature reaches 2100 K. Grodent & Gérard (2001) proposed two atmosphere models based on Voyager and Galileo data. They solved a diffusion equation in auroral conditions and obtained one model describing the atmosphere in a diffuse aurora and a second one describing a discrete aurora. Parkinson et al. (2006) also made models based on these data. We tested different models (see Sect. 3.5.3). In this paper, we present results obtained with the model of Grodent & Gérard (2001) for a discrete aurora (see Fig. 1).

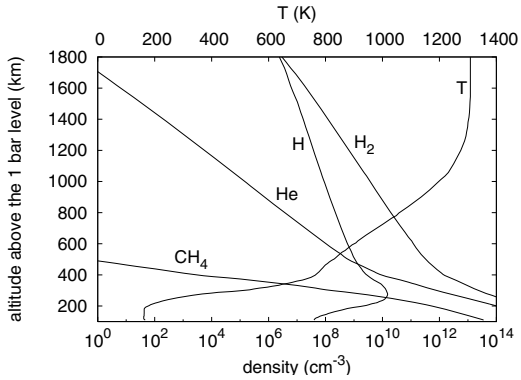

Fig. 1. Composition and temperature profiles in the atmosphere of a discrete aurora, after Grodent & Gérard (2001).

All the results shown here were obtained for an angle of 78° between the magnetic field line and the horizon, corresponding to a dipole magnetic angle at a latitude of 70°.

2.2. Effect of the solar EUV/FUV flux

The solar UV flux excites, ionizes and dissociates the neutral constituents of the atmosphere. We calculated the corresponding photoreaction rates.

2.2.1. Solar UV flux model

One energy input in our model is the solar EUV/FUV flux between 1.9 and 105 nm. We describe this spectrum using 39 wavelength bins, including 17 solar lines. In these bins we use the reference flux of Torr & Torr (1985) and Tobiska (1991). The solar spectrum is calibrated for two values ot the proxy $F10.7$, which is the value of the solar radio flux at 10.7 cm measured in 10^{22} W m^{-2}Hz^{-1}, and can be used as an indicator of the UV activity of the sun. These reference values are $F10.7 = 68$ (low solar activity) and $F10.7 = 243$ (active sun). A simple linear interpolation provides the flux at other activity levels.

2.2.2. Photoabsorption

The solar flux is absorbed by the constituents of the neutral atmosphere. The photoabsorption cross sections are given in Table 1.

The ionization and dissociation cross sections are listed in Table 2. We neglect the kinetic energy of the ion created during a photoionization. The photoelectron energy is thus $E = h\nu - W$,

Table 1. References for photoabsorption cross sections.

Species	References
H	Samson (1966)
H_2	Chung et al. (1993)
He	Yan et al. (1998)
CH_4	Samson et al. (1989) and Au et al. (1993)

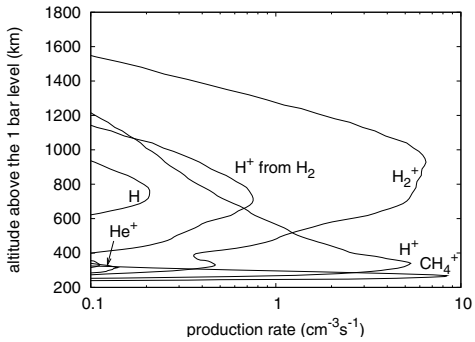

Fig. 2. Photoionization rates for a solar zenith angle of 70° and $F10.7 = 100$.

where $h\nu$ is the energy of the photon and W the ionization threshold. The photoelectron direction is arbitrary; we model it with an isotropic distribution.

2.2.3. Photoionization results

The solar UV processes play a minor role in the global ionization balance. Even at solar maximum, the solar UV flux is 1.36×10^{11} eV s^{-1} cm^{-2}, more than one order of magnitude smaller than the auroral electron flux. The UV photons pull a few 10^8 photoelectrons cm^{-2} s^{-1} out of the neutral atmosphere, 3 orders of magnitude less than the electrons precipitating in an auroral discrete arc.

In Fig. 2 we present the results for a moderate solar activity: $F10.7 = 100$, with a solar zenith angle of 70°. In the upper atmosphere, the simple ionization of H_2 is the dominant photoionization process. By absorbing the flux between 40 nm and 80.5 nm (its ionization threshold), H_2 produces up to 6.5 electrons cm^{-3} s^{-1} at the altitude of 910 km. In a lower layer H absorbs the UV photons which have not been absorbed by H_2 between 80.5 nm and H ionization threshold at 91.2 nm. This produces a secondary maximum of 5.4 electrons cm^{-3} s^{-1}. Eventually in the CH_4 layer in the bottom of our atmosphere, CH_4 ionization rate peaks at 8.4 cm^{-3} s^{-1} at 260 km.

This can be interpreted by looking at the penetration of the solar flux in the atmosphere. In Fig. 3 we present the solar flux arriving at different altitudes. We can see that H_2 ionization processes absorb the solar photons between 40 and 80 nm in the upper atmosphere. Lower in the atmosphere, H ionization absorbs more energetic photons, up to 10 nm. In the lower layer, methane, which has a low ionization threshold of 12.6 eV, is ionized by the low energy photons, which have not been absorbed in the upper atmosphere.

Compared to the charged particles precipitating at high latitude, the solar photons play a minor role in the auroral ionosphere. But at low latitude the solar flux is the main source of ionization of the atmospheric species. When the solar zenith angle decreases, the photons cross a thinner layer of atmosphere to arrive to a given altitude. So the solar flux is less absorbed and can ionize deeper. Figure 4 shows the photoionization rates when

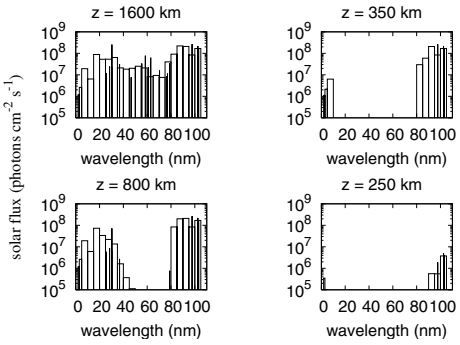

Fig. 3. Penetration of the solar UV flux in the atmosphere of Jupiter for a solar activity of $F10.7 = 100$ and a solar zenith angle of 70°.

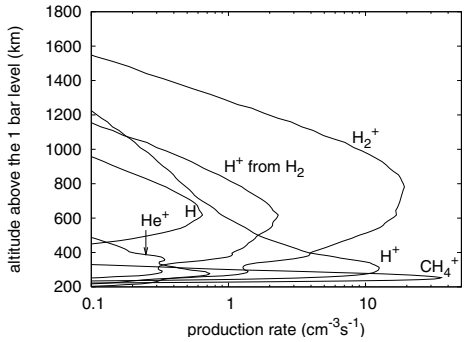

Fig. 4. Photoionization rates for a solar zenith angle of 0° and $F10.7 = 100$.

the sun is at zenith. In this case the photoionization layers of H_2 and H have gone respectively down to 700 and 300 km, and the ionization rates have been multiplied by a factor of roughly 3.

In the following, we set the solar activity to $F10.7 = 100$ and the solar zenith angle to 70°.

2.3. Auroral electron precipitation

2.3.1. Collisions between the auroral electrons and the atmospheric neutral species

The second energy input is the incident electron flux on top of the atmosphere. Its energy spectrum is still not determined. The Energetic Particle Detector on Galileo detected energetic electrons (15 keV $< E <$ 884 keV) between 10 and 25 jovian radii. But their energy distribution was not measured. The only in situ measurement of an electron energy distribution was done by Ulysses even further from Jupiter. The energy of the electrons precipitating in polar regions was evaluated through the analysis of color ratios in UV spectra of the main oval. In this way, Gustin et al. (2004) detected electrons with energies varying between 30 and 200 keV. Ajello et al. (2005) indicated the presence of electrons with energies of ~100 eV. Since there is a lack of more precise data, we studied precipitation with a Maxwellian spectrum centred at E_{maxw}, with E_{maxw} ranging from 100 eV to 150 keV.

The angular distribution of the precipitation is unknown as well. We show here results obtained with electrons precipitating parallel to the magnetic field lines on top of the atmosphere. But the code allows to modify this angular distribution and we tested the sensitivity of the results to this parameter (see Sect. 3.5.1).

By colliding with the neutral constituents of the atmosphere, the incident electrons are either elastically scattered or they excite or ionize the neutrals. Given the lack of data concerning the

Table 2. Photoionization and photodissociation reactions.

Species	Process	Threshold (eV)	References for cross sections
H	ionization	13.6	Samson (1966), Norwood et al. (1990)
H_2	ionization	15.4	Chung et al. (1993), Yan et al. (1998), Yan et al. (2001)
	dissociative ionization	18.1	Chung et al. (1993)
	dissociation	~25	Glass-Maujean & Schmoranzer (2005)
He	ionization	24.6	Yan et al. (1998)
	double ionization	79.0	Samson et al. (1992)
CH_4	ionization	12.6	Samson et al. (1989)
	dissociative ionizations	14.3 and 15.7	Samson et al. (1989)

Table 3. Electron impact reactions.

Species	Processes	References
H	elastic scattering	Kingston & Walters (1980), Shyn & Cho (1989), Shyn & Grafe (1992)
	H(2s)	Janev et al. (1987)
	H(2p)	James et al. (1997)
	n = 3, 4, 5, 6	Janev et al. (1987)
	H^+	Shah et al. (1987)
H_2	elastic scattering	Jain & Baluja (1992), Muse et al. (2008)
	rotation	Dalgarno et al. (1999)
	v = 1, 2	Janev et al. (1987)
	$B\,^1\Sigma_u^+$, $B'\,1\Sigma_u^+$, $B''\,1\Sigma_u^+$	Dalgarno et al. (1999)
	$C\,^1\Pi_u^+$	"
	$D\,^1\Pi_u$, $D'\,^1\Pi_u$	"
	E, $F\,^1\Sigma_g^+$	"
	$a^3\Sigma_g^+$, $b\,^3\Sigma_u^+$, $c\,^3\Pi_u$	Janev et al. (1987)
	higher excited states	Dalgarno et al. (1999)
	H^+	Liu & Shemansky (2004)
	H_2^+	Janev et al. (1987)
He	elastic scattering	Porter et al. (1987)
	2^3S, 2^1S, 2^3P, 2^1P,	Ralchenko et al. (2008)
	3^3S, 3^1S, 3^3P, 3^1P, 3^3D, 3^1D,	"
	4^3S, 4^1S, 4^3P, 4^1P, 4^3D, 4^1D, 4^3F, 4^1F	"
	He^+	"
	He^{++}	Pindzola et al. (2007)
CH_4	elastic scattering	Davies et al. (1989)
	v = 1, 2, 3, 4	"
	dissociation states	"
	CH_4^+, CH_3^+, CH_2^+	Liu & Shemansky (2006)

phase function which describes the elastic scattering of electrons by the hydrogen molecule, the elastic scattering of low energy electrons is described by the phase function given by Porter et al. (1987). This function is accurate for scattering by nitrogen but tests with other phase functions showed that it does not change the results of more than 3%. The excitation and ionization of the neutral atmospheric species are modelled by using electron impact cross sections, whose references are listed in Table 3.

The direction and the energy of the secondary electrons, which are produced through the ionization of the neutrals, depend on those of the incident electrons. They are assessed by using differential cross sections (Rees et al. 1969).

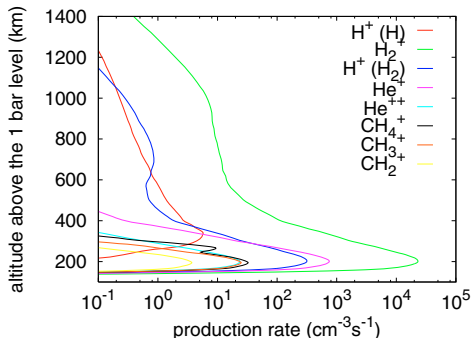

Fig. 5. Ionization rates for a Maxwellian precipitation of 50 keV.

2.3.2. Ionization rates

The ionization rates are presented in Fig. 5 for an electron Maxwellian precipitation with a characteristic energy E_{maxw} = 50 keV. The energy carried by the electron flux was set to 11 erg cm^{-2} s^{-1}. Using this value enabled Perry et al. (1999) to reproduce the H_2 Lyman band intensity. The collisions with the suprathermal electrons extract a total of 1.86×10^{11} electrons cm^{-2} s^{-1} by ionizing the neutral constituents of one atmospheric column (see Table 4). Most of this production is located at altitudes between 165 and 300 km.

The electron production is maximum at 200 km, where it reaches 2.43×10^4 electrons cm^{-3} s^{-1}. This production is mainly due to H_2 simple ionization, which produces a total of 1.78×10^{11} electrons cm^{-2} s^{-1} integrated on the atmospheric column.

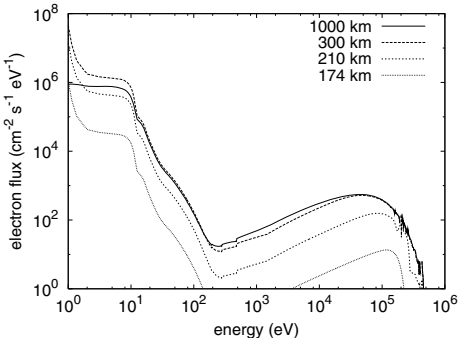

Fig. 6. Evolution of the electron flux with altitude in a night-side aurora. On top of the atmosphere the spectrum is a Maxwellian at 50 keV.

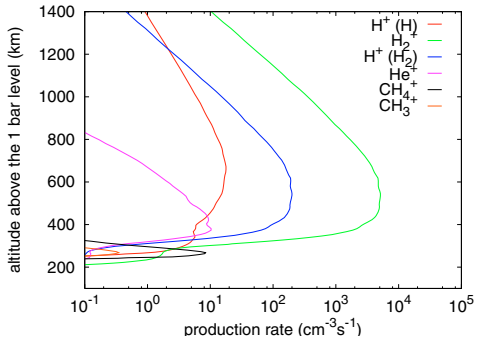

Fig. 7. Ionization rates for a Maxwellian precipitation of 1 keV.

The simple ionization of helium is the second most important reaction. However, with a total of 5.08×10^9 electrons cm^{-2} s^{-1}, it remains more than one order of magnitude less important than H_2 ionization, and is significant mainly in a thin layer around 200 km altitude. H^+ is produced in comparable quantity (2.50×10^9 cm^{-2} s^{-1}) and comes mainly from H_2 dissociative ionization. CH_4 ionization produces efficiently CH_4^+, CH_3^+ and even CH_2^+ around 195 km.

The interaction between the electron precipitation and the jovian atmosphere can be further investigated by looking at the altitude dependance of the energy spectrum of the precipitation. In Fig. 6 we plotted the total electron flux at different altitudes integrated on the pitch angles.

An intense flux of low-energy secondary electrons ($E <$ 100 eV) is present on top of the atmosphere. The flux of high-energy electrons does not change much above 300 km, it is just slightly reinforced by a few upwards secondaries. The stability of the high-energy flux is due to the weakness of the interaction between the neutrals and the high-energy electrons; actually the cross section quickly decreases above 200 eV. Below 300 km the density becomes strong enough, so that electrons are strongly absorbed thoughout the spectrum, particularly by CH_4 whose cross section is remarkably high compared to other constituent species.

Since we do not know the energy of the precipitating electrons, we varied the value of this parameter to see how it influences ionization rates and Lyman α emission. We considered Maxwellian precipitation from 100 eV to 150 keV, carrying the same energy flux of 11 erg cm^{-2} s^{-1}. The total amount of electrons stripped from the auroral atmosphere varies slowly, going from 1.57×10^{11} for electrons of 100 eV, up to 2.19×10^{11} cm^{-2} s^{-1} for electrons of 10 keV and then back down to 1.52×10^{11} for electrons of 150 keV. Under 20 keV, the ionization rates are very sensitive to the Maxwellian energy. In Fig. 7 we present ionization rate profiles for a Maxwellian precipitation of 1 keV. Except for methane, which is confined in the lowest layer of our model atmosphere, ionization occurs now higher than for the 50 keV precipitation: the electron production rate has a broad maximum around 530 km. Concerning high energy precipitation, since the cross sections decrease above 200 eV, the fastest electrons interact less and penetrate deeper in the atmosphere. Actually the change is fairly slow: the ionization rate peak goes down of only 70 km when the energy of the precipitation increases from 20 to 150 keV.

The results of TRANS* are comparable to those of the multi-stream code of Perry et al. (1999) (see Table 4). Their ionization rate profiles are shifted upwards but this is due to a shift between our atmospheric models. For a Maxwellian precipitation of 50 keV, they evaluated a total production of 1.83×10^{11} electrons cm^{-2} s^{-1}, which represents a difference of only 2% with the TRANS* prediction. If we run our code with their atmospheric model, we find again very similar ionization rates (within 10%). The main difference is that their ionization maximum is 50 km above ours.

We also compare our results with those of the 2-stream code of Grodent & Gérard (2001) and of the Monte-Carlo code of Hiraki & Tao (2008). Both use the triple Maxwellian proposed by Grodent & Gérard (2001) to simulate the electron flux in a discrete aurora:

$$\Phi(E) = \Phi_1 \frac{E}{E_1} e^{-\frac{E}{E_1}} + \Phi_2 \frac{E}{E_2} e^{-\frac{E}{E_2}} + \Phi_3 \frac{E}{E_3} e^{-\frac{E}{E_3}}$$

where $\Phi_1 = 100$ erg cm^{-2} s^{-1}, $E_1 = 22$ keV, $\Phi_2 = 10$ erg cm^{-2} s^{-1}, $E_1 = 3$ keV, $\Phi_3 = 0.5$ erg cm^{-2} s^{-1}, $E_1 = 100$ eV. The following H_2^+ production profiles are presented in Fig. 8. The profiles compare quite well. Our profile is more peaked than previous works. The use of different numerical schemes, cross sections and angular discretization are enough to explain the differences between theses studies.

2.3.3. Energy balance

In our simulations the total energy input in the atmosphere is 7.06×10^{12} eV cm^{-2} s^{-1}. In the case of a Maxwellian precipitation of 50 keV, 97% of this energy is transferred to the atmosphere through inelastic collisions. 3% goes back to space through electron escape. A minor fraction of ~0.05% is used to heat the ionosphere through friction between the suprathermal electrons and the thermalized ionospheric electrons.

The conversion into heat is more effective with low-energy precipitation. For a precipitation of 1 keV (resp. 100 eV), 4% (resp. 9%) of the input energy goes to heating. This is smaller than the 18.8% found by the 2-stream code of Waite et al. (1983) for a 1 keV precipitation and than the 50% found by Grodent for precipitation with a wide spectrum ranging from 100 eV to 22 keV. Low-energy precipitation could neverthless contribute to explain the high temperatures of the jovian auroral thermosphere.

3. Lyman α line

3.1. Lyman α transition

This line corresponds to the radiative de-excitation H(2p) $\rightarrow$ H(1s) at 1215.67 nm. H(2s) $\rightarrow$ H(1s) is a forbidden dipolar transition. Consequently H(2s) is metastable and it has a long life-time ($\tau = 0.14$ s, to be compared to 1.6 ns

Table 4. Column ionization rates for electron precipitation with Maxwellian spectra of different characteristic energies.

Species	This work		Perry et al. (1999)
	1 keV	50 keV	50 keV
e^-	2.00×10^{11}	1.86×10^{11}	1.83×10^{11}
H^+ from H	8.57×10^{8}	1.03×10^{7}	2.38×10^{7}
H_2^+	1.92×10^{11}	1.78×10^{11}	1.70×10^{11}
H^+ from H_2	7.59×10^{9}	2.49×10^{9}	6.74×10^{9}
He^+	1.89×10^{8}	5.08×10^{9}	6.12×10^{9}
He^{++}	1.28×10^{7}	1.57×10^{8}	
CH_4^+	5.57×10^{3}	1.80×10^{8}	6.12×10^{7}
CH_3^+	4.28×10^{3}	1.38×10^{8}	5.84×10^{7}
CH_2^+	7.21×10^{2}	2.05×10^{7}	8.28×10^{6}
H (neutral dissociation of H_2)	1.18×10^{11}	1.12×10^{11}	

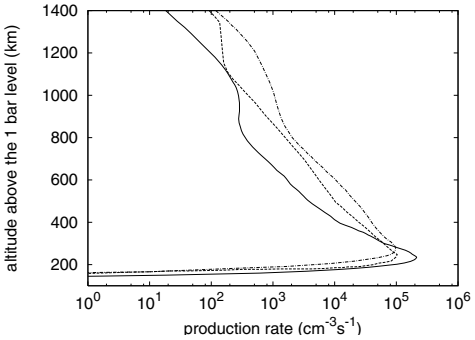

Fig. 8. H_2^+ production rates for electron precipitation with a triple Maxwellian spectrum. Full line: our results. Dashed-dotted line: Grodent & Gérard (2001). Dashed line: Hiraki & Tao (2008).

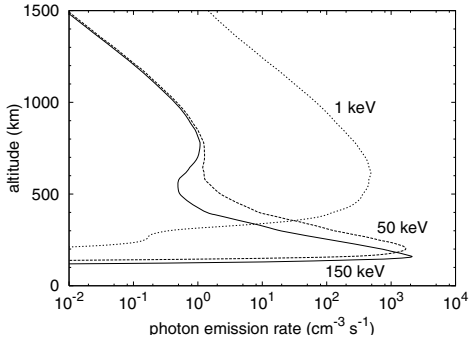

Fig. 9. Emission rate of Lyman Alpha photons, at low solar illuminance ($F10.7 = 100$, solar zenith angle of 70°) and Maxwellian precipitation of 1 keV, 50 keV and 150 keV.

for H(2p)). The spontaneous decay of H(2s) to H(1s) is a 2-photon transition which does not contribute to Lyman α (Slocomb et al. 1971). But the energy difference between H(2s) and H(2p) is very small, and H can go from one state to the other when it collides with another particle. So if the atmosphere is dense enough, this collisional quenching makes H(2s) deexcite via H(2p) and a Lyman α photon. For particles with thermal velocity (v_{th} ~ a few km s^{-1} in the atmosphere of Jupiter), the cross section for collisional quenching of H(2s) by collisions with H_2 is $\sigma_{quench} \sim 100$ Å^2 (Vassilev et al. 1990). The collisional lifetime of H(2s) can thus be evaluated by $\tau_{coll} = \frac{1}{n\sigma_{quench}v_{th}}$, where n is the density of H_2. It is shorter than the spontaneous lifetime for altitudes higher than 1300 km. Given that the Lyman α emission in Jupiter's atmosphere occurs mainly below this altitude, we consider that every atom excited in the H(2s) state deexcites by emitting a Lyman α photon after a collisional quenching.

3.2. Lyman α emission

Two phenomena contribute to the Lyman α emission of Jupiter's auroral atmosphere: the diffusion of the solar Lyman α flux and the emission by atmospheric H atoms. We evaluate the latter with TRANS*: the profile of the excitation rate of H($n = 2$) is represented in Fig. 9, where the atmosphere is lit by the solar UV flux and struck by a precipitation of 50-keV electrons. It takes into account the excitation of H atoms as well as the dissociation of H_2 and CH_4 molecules (although the contribution of CH_4 is negligible). The cross sections are listed in Table 5.

The solar excitation leads to a faint Lyman α emission around 850 km. The main Lyman α emission is due to electron precipitation. It is at the same altitude as the H_2 ionization rate maximum (which is normal because the cross sections have comparable shapes).

3.3. Radiative transfer at Lyman α

The emitted photons are scattered resonantly by Jupiter's atmospheric H. A radiative transfer code is used to calculate the emergent intensity and line profile. This code is described in Griffioen (2000), Parkinson (2002) and Barthélemy et al. (2004). It models scattering and absorption of the solar Lyman α line and of the Lyman α photons emitted by the excited atmospheric hydrogen. This pseudo-1D code allows for a solar zenith angle varying along the line of sight and is based on the Feautrier method. The line profiles are based on Voigt profiles and scattering is modelled with the use of redistribution functions. The angular scattering is supposed to be isotropic. Due to the Doppler effect linked with the motion of the atmospheric particles, the absorbed photons are reemitted with a slightly different frequency (described by the redistribution function). So if the photons are emitted deep enough, multiple scattering depletes the core of the line when it emerges out of the atmosphere. The depletion does not happen in the wings where the photons are not resonant with Lyman α and the atmosphere is optically thin. The choice of the frequency redistribution function is not obvious. If the excited H atoms collide with another particle before they de-excite and emit a photon, the complete frequency redistribution (CFR) function should be used. On the contrary, if the atmosphere is more diluted, the angle-averaged redistribution (AAPR) is best suited (Rego et al. 1999). By taking a collision cross section of 100 Å^2, we evaluate that the characteristic time between two

Table 5. References for cross sections for production of Lyman α photons by electronic collision and photoexcitation.

Process	References
Electron collisions:	
H(1s) → H(2s)	Janev et al. (1987)
H(1s) → H(2p)	James et al. (1997)
H_2 → Lyman α	Ajello et al. (1991)
CH_4 → Lyman α	Pang et al. (1987)
Photoexcitation:	
H_2 → Lyman α	Bozek et al. (2006)
CH_4 → Lyman α	Wu & Judge (1981), Fukuzawa et al. (2005)

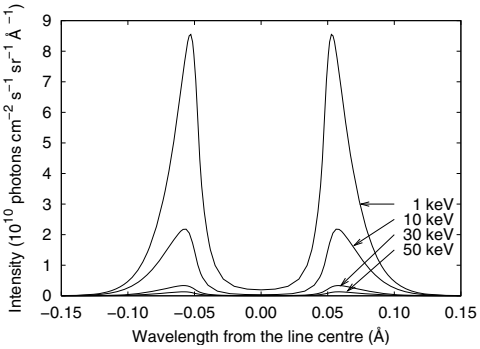

Fig. 10. Profile of the Lyman α line for different electron energies E_{maxw}. The electrons precipitate parallel to the magnetic field lines.

collisions is $\gtrsim$1 ms. This is much longer than the lifetime of the level H(2p), so we choose to use the AAPR function.

3.4. Results

3.4.1. Night side aurora

We studied the Lyman α line for electron precipitation with characteristic energies E_{maxw} ranging from 100 eV to 150 keV. In Fig. 10 we present the shape of the Lyman α line for a few values of E_{maxw}, in a night-side aurora. The line of sight is parallel to the Jupiter-sun direction and intersects Jupiter's rotation axis at the latitude of 70°. In the code, we can choose the line of sight but we keep it fixed since in this paper we do not compare our results with observations. The main characteristics of the line is a strong reversal at its centre. It is due to the resonant scattering of the auroral Lyman α photons. It has been observed in auroral spectra taken by the Goddard High Resolution Spectrograph (Prangé et al. 1997).

For the most energetic electrons, the Lyman α emission occurs very low in the atmosphere and the line is strongly absorbed before emerging out of the atmosphere. Hence, the intensity of the line decreases when the electron energy increases. However, a measurement of the intensity can not be used to determine the energy of the electrons since we do not know the energy input flux in the jovian aurorae.

Other properties of the line have to be used to characterise the electrons: its *FWHM*, the width of its reversal $\delta\lambda$ (defined as the distance between the two peaks) and the intensity of its reversal R_{rev} (defined as the ratio of peaks value to reversal center). These characteristics are given in Table 6 for different electron energies.

In the 100 eV−10 keV energy range, the line width and the width and the intensity of the reversal increase with E_{maxw}. So by measuring these parameters in a spectrum with a resolution of 11 mÅ like that of STIS, it should be possible to constrain the energy of the electrons at low energy, where the variations are the fastest. It is no longer the case above 30 keV where the parameters are quite constant. Observing only the Lyman α line is not a good way to characterise electrons above 30 keV on the night side.

Table 6. Properties of the Lyman α line for different electron energies E_{maxw} on the night side of the auroral oval.

E_{maxw} (keV)	I_{tot} (kR)	*FWHM* (mÅ)	$\delta\lambda$ (mÅ)	R_{rev}
0.1	101	113	97	21
1	63.2	137	105	44
10	14.9	156	117	61
30	3.02	158	117	62
50	1.18	158	117	62
100	0.385	159	118	63
150	0.174	159	118	63

Our results are qualitatively comparable to those of Rego et al. (1999), but quantitatively they differ. Our lines are narrower and our reversal is narrower and less pronounced. It can be linked with differences in the atmospheric models. On top of the atmosphere, H density is 33 times larger in their model than in ours and on the bottom of the atmosphere, it is 3 times larger in our model. The smaller H density in our model makes the frequency redistribution less important and the line narrower.

3.4.2. Day side aurora

In a day side aurora, two sources contribute to the Lyman α emission: the scattering of the solar light and the emissions by the atmospheric particles. The incident solar line is modelled by a double Gaussian profile:

$$\pi F(f) = \frac{\pi F}{2\sqrt{\pi} f_0}\left(e^{-\left(\frac{f-f_1}{f_0}\right)^2} + e^{-\left(\frac{f+f_1}{f_0}\right)^2}\right)$$

where f is the frequency, πF the Lyman α flux incident on top of the atmosphere, f_0 the dispersion and f_1 the offset. We take the same values as Gladstone (1988) and Parkinson et al. (1999): f_0 = 214.6 mÅ and f_1 = 219.24 mÅ. We adapt the value of πF to the activity of the sun: $\pi F = 1.35 \times 10^{10}$ photons cm^{-2} s^{-1} for $F10.7$ = 100 and $\pi F = 2.02 \times 10^{10}$ photons cm^{-2} s^{-1} for $F10.7$ = 240 (Lemaire et al. 2002).

The profiles in Fig. 11 were obtained for a moderate solar activity ($f10.7$ = 100). The line of sight and the physical conditions are similar to those of the Fig. 10. At high energy we can easily distinguish the contribution from the solar scattered line and that from the auroral emissions. Compared to the night side, the intensity of the line increases, from a factor 1.01 at 100 eV to a factor 50.9 at 150 keV. R_{rev} decreases, particularly at high energy; the centre of the line becomes brighter than the peaks above 130 keV. The *FWHM* and the distance between the peaks are unchanged at low energy. At high energy, the solar line determines the final profile. The resultant line is broader and the peaks are a bit closer than on the night side: at 150 keV, the *FWHM* is multiplied by 2.13 and $\delta\lambda$ is divided by 1.20. All these changes are amplified if the solar activity is higher (see the dashed line in Fig. 11(b) where $f10.7$ = 240.

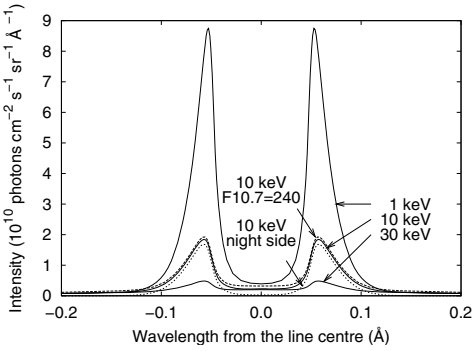

(a) Low-energy precipitation

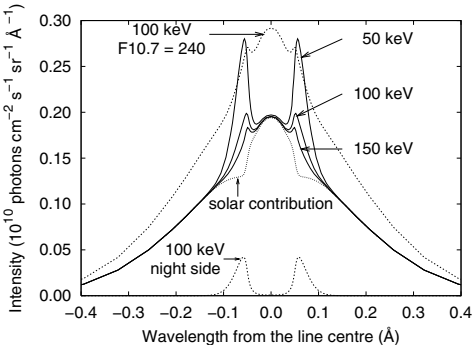

(b) High-energy precipitation

Fig. 11. Profile of the Lyman α line on the day side aurora for different electrons energies and for a moderate solar activity ($F10.7 = 100$). For comparison, the dotted lines represent the profiles on the night side and the dashed lines the profile on the day side for a strong solar activity ($F10.7 = 240$). The solar reflected line is also represented (dotted) for $F10.7 = 100$.

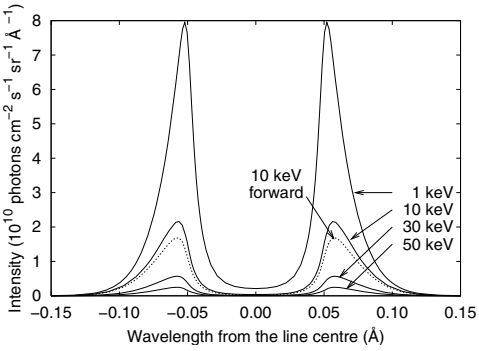

Fig. 12. Profile of the Lyman α line on the night side for an isotropic incident flux of electrons. For comparison, the dotted line shows the line for electron precipitation of 10 keV parallel to the magnetic field. The Gaussian case is not illustrated here; its results are intermediate between the isotropic and the forward cases.

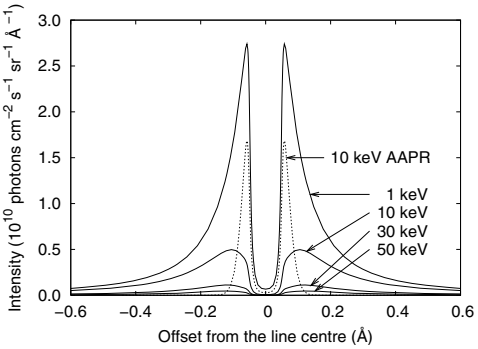

Fig. 13. Profile of the Lyman α line obtained on the night side with the CR function. The dotted line was obtained with the AAPR function.

3.5. Sensitivity study

3.5.1. Angular distribution of the precipitating electrons

In the results presented above, the precipitation is parallel to the magnetic field lines. But we also made simulations with different angular distributions: we imposed isotropic or Gaussian incident fluxes on top of the atmosphere. For these latter, the atmospheric layer where H($n = 2$) get excited is slightly higher in the atmosphere (of 30 km). The excitation is also a bit less effective (it goes down of 10−20% at the altitude where it is maximum). But these changes have a small impact on the Lyman α profile because the low-energy secondary electrons, whose direction is almost independant from that of the initial precipitation, play a major role in the production of excited H($n = 2$). The corresponding line is represented in Fig. 12. The biggest change is the depth of the reversal at the lowest energies where it varies up to 20%. The *FWHM* and the width of the reversal vary by less than 4%. So the observation of the Lyman α line will not easily allow us to deduce the angular distribution of the precipitating particles. But Prangé et al. (1995) showed that a color ratio in H_2 Lyman and Werner lines depends on it. So the observation of H_2 lines seems to be a better way to constrain the angular distribution of the precipitation.

In the following, we keep the incident electron flux parallel to the magnetic field lines.

3.5.2. Redistribution function

So far, we have presented results obtained with the angle averaged partial redistribution function (AAPR). But we also ran the code with the complete redistribution function (CFR), which is suited if the medium is very collisional, such as those that occur below ~200 km in Jupiter's atmosphere. The results are presented in Fig. 13. The peaks are much less intense; most of the flux is contained in the wings, which extend much further. The *FWHM* increases up to 3.4 times for the highest energies. The distance between the peaks increases up to 2.1 times. $R_{\rm rev}$ increases at high energy (up to 22%).

3.5.3. Atmosphere model

To check the sensitivity of our results to atmospheric models, we run our codes with an atmosphere based on the work of Trafton et al. (1994). This model was built after the analysis of CH_4, H_2 and H_3^+ lines in spectra of Jupiter's aurorae. The authors built a chemical model which allowed them to reproduce lines of H_2, H_3^+ and hydrocarbons. The results are illustrated in Fig. 14. In Trafton's model, the density of H is reduced, leading to less redistribution and a narrower line with a less pronounced reversal. This variation goes in the same sense than the difference between our results and those of Rego et al. (1999).

4. Conclusion

We modelled the impact of the solar UV flux and of the precipitation of electrons in the atmosphere of Jupiter. To do so we used

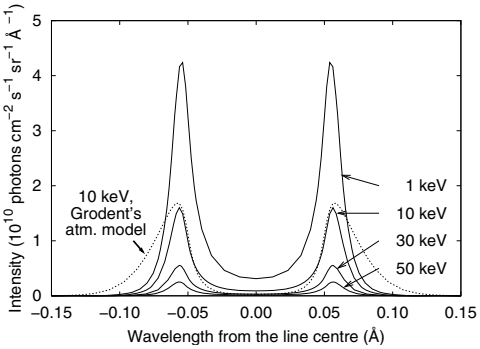

Fig. 14. Lyman α line obtained on the night side with the atmospheric model of Trafton et al. (1994). For comparison, the dotted line shows the results obtained with our reference model (Grodent & Gérard 2001).

a multi-stream code which solves the Boltzmann equation. We calculated the photoionization rates of H, H_2, He and CH_4. The photoionization is significant at 260 km due to methane and between 800 and 900 km (depending on the solar zenith angle) due to H_2. We also calculated the ionization rates due to the precipitation of electrons in Jupiter's aurorae. We modelled the incident flux of electrons by a Maxwellian spectrum with a characteristic energy ranging from 100 eV to 150 keV and carrying a total energy flux of 11 erg cm^{-2} s^{-1}. The ionization rate due to electron precipitation is 2 orders of magnitude larger than that due to the solar UV flux. The altitude of the ionization layers goes from 1040 km to 165 km when the energy of the Maxwellian goes from 100 eV to 150 keV. We calculated the Lyman α photon emission rate using a radiative transfer code to model the profile of the line emergent out of the atmosphere. Due to the frequency redistribution which happens during scattering, the core of the line is depleted, with photons moving out to the wings. The line profile can be used to constrain the energy of the precipitation only if the latter is inferior to ~10 keV. We tested the sensitivity of the results to different input parameters and found that the initial angular distribution of the precipitation has little influence on the results. On the contrary, the line depends critically on the choice of the frequency redistribution function and on the atmosphere model. In a next paper we will model the Lyman and Werner bands of H_2 in order to get further constraints on the electron precipitation. Later we will compare our calculations with HST spectra. That work will then be adapted to the study of exoplanets' aurorae to assess if their H_2 auroral emissions are likely to be observed from earth.

References

Ajello, J. M., James, G. K., & Shemansky, D. E. 1991, ApJ, 371, 422
Ajello, J. M., Pryor, W., Esposito, L., et al. 2005, Icarus, 178, 327
Au, J. W., Cooper, G., Burton, G. R., & Olney, Terry N., B. C. E. 1993, Chem. Phys., 173(2), 209
Barthélemy, M., Parkinson, C., Lilensten, J., & Prangé, R. 2004, A&A, 423, 391
Ben Jaffel, L., Kim, Y. J., & Clarke, J. 2007, Icarus, 190, 504
Bozek, J. D., Furst, J. E., Gay, T. J., et al. 2006, J. Phys. B: Atomic (Molecular and Optical Physics), 39, 4871
Chung, Y. M., Lee, E.-M., Masuoka, T., & Samson, J. A. R. 1993, J. Chem. Phys., 99, 885
Dalgarno, A., Yan, M., & Liu, W. 1999, ApJS, 125, 237
Davies, D. K., Kline, L. E., & Bies, W. E. 1989, J. Appl. Phys., 65, 3311
Fukuzawa, H., Odagiri, T., Nakazato, T., et al. 2005, J. Phys. B: Atomic Molecular and Optical Physics, 38, 565
Gladstone, G. R. 1988, J. Geophys. Res., 93, 14623
Glass-Maujean, M., & Schmoranzer, H. 2005, J. Phys. B: Atomic Molecular and Optical Physics, 38, 1093
Griffioen, E. 2000, J. Geophys. Res., 105, 24613
Grodent, D., & Gérard, J.-C. 2001, J. Geophys. Res., 106, 12933
Gronoff, G., Lilensten, J., Simon, C., et al. 2008, A&A, 482, 1015
Gustin, J., Gérard, J.-C., Grodent, D., et al. 2004, J. Geophys. Res. (Space Physics), 109, 10205
Hiraki, Y., & Tao, C. 2008, Annales Geophysicae, 26, 77
Jain, A., & Baluja, K. L. 1992, Phys. Rev. A, 45, 202
James, G. K., Slevin, J. A., Shemansky, D. E., et al. 1997, Phys. Rev. A, 55, 1069
Janev, R. K., Langer, W. D., Post, Jr., D. E., & Evans, K. J. 1987, Shock and Vibration, 4
Kingston, A. E., & Walters, H. R. J. 1980, J. Phys. B: Atomic and Molecular Physics, 13, 4633
Lemaire, P., Emerich, C., Vial, J.-C., et al. 2002, From Solar Min to Max: Half a Solar Cycle with SOHO, ed. A. Wilson, ESA SP-508, 219
Lilensten, J., & Blelly, P. L. 2002, J. Atmosph. Solar-Terrestr. Phys., 64, 775
Lilensten, J., Simon, C., Witasse, O., et al. 2005, Icarus, 174, 285
Liu, X., & Shemansky, D. E. 2004, ApJ, 614, 1132
Liu, X., & Shemansky, D. E. 2006, J. Geophys. Res. (Space Physics), 111, 4303
Miller, S., Achilleos, N., Ballester, G. E., et al. 2000, Roy. Soc. Lond. Phil. Trans. Ser. A, 358, 2485
Muse, J., Silva, H., Lopes, M. C. A., & Khakoo, M. A. 2008, J. Phys. B: Atomic, Molecular and Optical Physics, 41, 095203 (7pp)
Norwood, K., Ng, C. Y., & Vary, J. P. 1990, J. Chem. Phys., 93, 1480
Pang, K. D., Ajello, J. M., Franklin, B., & Shemansky, D. E. 1987, J. Chem. Phys., 86, 2750
Parkinson, C. D. 2002, Ph.D. Thesis, AA (York University (Canada))
Parkinson, C. D., Griffioen, E., McConnell, J. C., et al. 1999, Geophys. Res. Lett., 26, 3177
Parkinson, C. D., Stewart, A. I. F., Wong, A. S., Yung, Y. L., & Ajello, J. M. 2006, J. Geophys. Res. (Planets), 111, 2002
Perry, J. J., Kim, Y. H., Fox, J. L., & Porter, H. S. 1999, J. Geophys. Res., 104, 16541
Pindzola, M. S., Robicheaux, F., & Colgan, J. 2007, Phys. Rev. A, 76, 024704
Porter, H. S., Varosi, F., & Mayr, H. G. 1987, J. Geophys. Res., 92, 5933
Prangé, R., Rego, D., & Gerard, J.-C. 1995, J. Geophys. Res., 100, 7513
Prangé, R., Rego, D., Pallier, L., et al. 1997, ApJ, 484, L169
Ralchenko, Y., Janev, R. K., Kato, T., et al. 2008, Atomic Data and Nuclear Data Tables, 94, 603
Rees, M. H., Stewart, A. I., & Walker, J. C. G. 1969, Planet. Space Sci., 17, 1997
Rego, D., Clarke, J. T., Ben Jaffel, L., et al. 2001, Icarus, 150, 234
Rego, D., Prangé, R., & Ben Jaffel, L. 1999, J. Geophys. Res., 104, 5939
Rego, D., Prange, R., & Gerard, J.-C. 1994, J. Geophys. Res., 99, 17075
Samson, J. A. R. 1966, Adv. Atom. Mol. Phys., 2, 177
Samson, J. A. R., Haddad, G. N., Masuoka, T., Pareek, P. N., & Kilcoyne, D. A. L. 1989, J. Chem. Phys., 90, 6925
Samson, J. A. R., Bartlett, R. J., & He, Z. X. 1992, Phys. Rev. A, 46, 7277
Seiff, A., Kirk, D. B., Knight, T. C. D., et al. 1998, J. Geophys. Res., 103, 22857
Shah, M. B., Elliott, D. S., & Gilbody, H. B. 1987, J. Phys. B: Atomic and Molecular Physics, 20, 3501
Shyn, T. W., & Cho, S. Y. 1989, Phys. Rev. A, 40, 1315
Shyn, T. W., & Grafe, A. 1992, Phys. Rev. A, 46, 2949
Slocomb, C. A., Miller, W. H., & III, H. F. S. 1971, J. Chem. Phys., 55, 926
Stallard, T., Miller, S., Millward, G., & Joseph, R. D. 2002, Icarus, 156, 498
Stamnes, K., & Rees, M. H. 1983, Geophys. Res. Lett., 10, 309
Tobiska, W. K. 1991, J. Atmosph. Terrestr. Phys., 53, 1005
Torr, M. R., & Torr, D. G. 1985, J. Geophys. Res., 90, 6675
Trafton, L. M., Dols, V., Gérard, J.-C., et al. 1998, ApJ, 507, 955
Trafton, L. M., Gerard, J. C., Munhoven, G., & Waite, Jr., J. H. 1994, ApJ, 421, 816
Vasavada, A. R., Bouchez, A. H., Ingersoll, A. P., et al. 1999, J. Geophys. Res., 104, 27133
Vassilev, G., Perales, F., Miniatura, C., et al. 1990, Z. Phys. D Atoms Molecules Clusters, 17, 101
Waite, J. H., Cravens, T. E., Kozyra, J., et al. 1983, J. Geophys. Res., 88, 6143
Wu, C. Y. R., & Judge, D. L. 1981, J. Chem. Phys., 75, 172
Yan, M., Sadeghpour, H. R., & Dalgarno, A. 1998, ApJ, 496, 1044
Yan, M., Sadeghpour, H. R., & Dalgarno, A. 2001, ApJ, 559, 1194
Young, R. E. 2003, New Astron. Rev., 47, 1